The Unfitted Discontinuous Galerkin Method for Solving the EEG Forward Problem: A Second Order Study

Andreas Nüßing, Carsten H. Wolters, Heinrich Brinck, Christian Engwer

***Abstract*—We present a study of the unfitted discontinuous Galerkin finite element method (UDG-FEM) for solving the electroencephalography forward problem (EEG) using second order polynomial functions. In [1] UDG-FEM was introduced as a method for solving the EEG forward problem. Convergence could be validated numerically and it performed similarly or even better than competitive methods on hexahedral or conforming tetrahedral meshes. The method in [1] used linear local polynomial spaces in its mathematical formulation. However, given a smooth level set representation of the different tissue boundaries, UDG-FEM can also be used with polynomials of higher order. We present a first evaluation of UDG-FEM with second order polynomials and compare it to the linear case. The results show that for the same number of degrees of freedom, second order polynomials achieve an overall higher accuracy than linear ones.**

***Index Terms*—Unfitted Discontinuous Galerkin, Finite Element Method, Second Order, EEG Forward Problem**

I. INTRODUCTION

The unfitted discontinuous Galerkin finite element method (UDG-FEM) as a method for discretizing partial differential equations was first introduced in [2]. In [1] UDG-FEM has been used to solve the electroencephalography forward problem (EEG). It showed an overall good accuracy when compared to competitive methods on conforming meshes, while providing a less complex simulation pipeline. In addition, it derived properties of the discontinuous Galerkin finite element method (DG-FEM), such as for example conservation properties on a discrete level. Locally, the discrete model employs polynomial basis functions. In [1], results where presented only for linear polynomials. For the standard finite element method (CG-FEM) with conforming tetrahedral meshes results for second order finite elements have been presented [3]–[5]. The accuracy could be increased, but the geometric representation has been identified as a possible error source.

This study focusses on comparing the results for UDG-FEM with first order functions to the ones obtained by using quadratic polynomials. As UDG-FEM uses level set functions for the representation of the model geometry, a better geometric representation of the smooth surfaces can be obtained, which can be beneficial for a second order method. In Section II, the UDG-FEM approach is recalled and extended to second order polynomials. Section III presents results of a comparison in four-layer sphere model which are discussed in Section IV. Finally, a short conclusion is given in Section V.

II. METHODS

A. An unfitted discontinuous Galerkin method

In the following, we will describe the unfitted discontinuous Galerkin finite element method (UDG-FEM) for solving the EEG forward problem. We will closely follow the description in [1] and note on the differences when introducing second order polynomials.

The EEG forward problem is solved by providing a solution to the inhomogeneous Poisson equation on the head domain $\Omega \subset \mathbb{R}^3$ with homogeneous Neumann boundary conditions, i.e.

$$\nabla \cdot \sigma \nabla u = f \quad \text{in } \Omega \tag{1}$$

$$\sigma \nabla u \cdot n = 0 \quad \text{in } \partial\Omega \tag{2}$$

$\sigma : \Omega \to \mathbb{R}^{3\times 3}$ denotes the symmetric and positive definite conductivity tensor. We will assume that the domain Ω is embedded in a larger domain $\hat{\Omega} \subset \mathbb{R}^3$. To derive a discrete model, we introduce a structured mesh $\mathcal{T}_h$ of this outer domain:

$$\mathcal{T}_h = \{E_i \subset \hat{\Omega} | i \in \mathcal{I} = \{0, \dots, N-1\}\} \tag{3}$$

$$E_i \cap E_j = \emptyset \;\forall i \neq j, \quad \bigcup_{i\in\mathcal{I}} \overline{E}_i = \overline{\hat{\Omega}} \tag{4}$$

of open sets $E_i \subset \mathbb{R}^3$. $h \in \mathbb{R}$ is defined as the mesh width, i.e., $h := \max\{\text{diam}(E) : E \in \mathcal{T}_h\}$. In the following, we will call this structured mesh *fundamental mesh*.

A way of describing the head domain Ω is to use a level set function. A level set function for Ω is a function $\Phi : \hat{\Omega} \to \mathbb{R}$ with the property

$$\Phi(x) \begin{cases} < 0 & , x \in \Omega \\ = 0 & , x \in \partial\Omega \\ > 0 & , x \in \hat{\Omega} \setminus \overline{\Omega} \end{cases} \tag{5}$$

On the fundamental mesh $\mathcal{T}_h$, the level set function is approximated as a piecewise multilinear $\mathbb{Q}_1$ function Φ_h by

---

Andreas Nüßing is with the Institute for Bioinformatics and Chemoinformatics, Westfälische Hochschule, Recklinghausen, Germany, with the Institute for Computational and Applied Mathematics, University of Münster, Germany and with the Institute for Biomagnetism and Biosignalanalysis, University of Münster, Germany.

Carsten H. Wolters is with the Institute for Biomagnetism and Biosignalanalysis, University of Münster, Germany.

Heinrich Brinck is with the Institute for Bioinformatics and Chemoinformatics, Westfälische Hochschule, Recklinghausen, Germany.

Christian Engwer is with the Institute for Computational and Applied Mathematics and the Cluster of Excellence EXC 1003, Cells in Motion, CiM, University of Münster, Germany.

evaluating Φ at each grid node. In order to provide a better geometric representation, we will also consider discrete level set functions defined on a finer mesh, which resulted from a regular global refinement of the fundamental mesh. By employing multiple level set functions $\Phi_h^0, \dots, \Phi_h^{L-1}$, we can differentiate between multiple domains. Each such level set function separates $\hat{\Omega}$ into two parts with respect to its sign. We will denote these parts by $\Omega_{i,-}$ and $\Omega_{i,+}$ for the negative and positive side of the level set function i. From these parts, we can create domains $\mathcal{D}_0, \dots, \mathcal{D}_{D-1}$, consisting of intersections of negative and positive sides of the level set functions, i.e. $\mathcal{D}_0, \dots, \mathcal{D}_{D-1} \subset \{\bigcap_{(i,p)\in I} \Omega_{i,p} : I \subset \{0, \dots, L-1\} \times \{-,+\}\}$. For a domain $\mathcal{D}_i$ we define its support as $\Omega(\mathcal{D}_i) := \bigcup \mathcal{D}_i$ and require that the supports of all domains are pairwise disjoint, i.e., $\Omega(\mathcal{D}_i) \cap \Omega(\mathcal{D}_j) = \emptyset$ holds for $i \neq j$. For each element E_i, we set its set of intersecting domains to $\mathcal{D}(E_i) := \{\mathcal{D}_j : E_i \cap \Omega(\mathcal{D}_j) \neq \emptyset\}$. From this domain information we generate a cut cell triangulation:

$$\overline{\mathcal{T}}_h = \bigcup_{E_i \in \mathcal{T}_h} \{\underbrace{E_i \cap \Omega(\mathcal{D}_j)}_{=:E_i^j} : \mathcal{D}_j \in \mathcal{D}(E_i)\} \tag{6}$$

The elements of this triangulation, i.e. the intersections of the fundamental mesh elements with the different domains are called cut cells. The skeleton $\overline{\Gamma}_h := \overline{\Gamma}_h^d \cup \overline{\Gamma}_h^e$ of $\overline{\mathcal{T}}_h$ is defined as the union of the inter-domain skeleton $\overline{\Gamma}_h^d := \{\gamma_i^{j,k} := \overline{E}_i^j \cap \overline{E}_i^k : E_i^j, E_i^k \in \overline{\mathcal{T}}_h, k \neq j, |\gamma_i^{j,k}| > 0\}$ and the inter-element skeleton $\overline{\Gamma}_h^e := \{\gamma_{i,j}^k := \overline{E}_i^k \cap \overline{E}_j^k : E_i^k, E_j^k \in \overline{\mathcal{T}}_h, i \neq j, |\gamma_{i,j}^k| > 0\}$. For simplicity reasons, we introduce a global cut cell numbering and denote the cut cells by $\overline{E}_0, \dots, \overline{E}_{N_c-1}$.

Let $V_h^k = \{u \in L_2(\Omega) : u|_E \in \mathcal{P}^k(E)\ \forall E \in \overline{\mathcal{T}}_h\}$ denote the broken polynomial space on $\overline{\mathcal{T}}_h$. $\mathcal{P}^k(E)$ denotes a space of polynomials on E of degree $k \in \mathbb{N}$. We will assume that σ is constant on each $\overline{E}_i \in \overline{\mathcal{T}}_h$ and denote its value by σ_i. The unfitted discontinuous Galerkin method for solving (1), which we will use, then reads: Find $u_h \in V_h^k$ such that

$$a(u_h, v_h) + J(u_h, v_h) = l(v_h) \quad \forall v_h \in V_h^k \tag{7}$$

holds. The bilinear forms a and J are given as

$$a(u_h, v_h) = \int_\Omega \sigma \nabla u_h \cdot \nabla v_h dx - \int_{\overline{\Gamma}_h} [\![u_h]\!] \langle \sigma \nabla v_h \rangle ds \tag{8}$$

$$- \int_{\overline{\Gamma}_h} [\![v_h]\!] \langle \sigma \nabla u_h \rangle ds \tag{9}$$

$$J(u_h, v_h) = \eta \int_{\overline{\Gamma}_h} \frac{\tau_\gamma \nu_k}{h_\gamma} [\![u_h]\!] [\![v_h]\!] ds \tag{10}$$

$$l(v_h) = \int_\Omega f v_h dx \tag{11}$$

The jump $[\![u_h]\!]$ on the intersection between two cut cells $\overline{E}_i$ and $\overline{E}_j$ with unit outer normals n_i and n_j, respectively, is defined as $[\![u_h]\!] := u_h|_{\overline{E}_i} n_i + u_h|_{E_j} n_j$. $\langle \sigma \nabla u_h \rangle$ denotes the weighted average of the flux of u_h on the interface. With $\delta_i := n_i^t \sigma_i n_i$ and $\delta_j := n_j^t \sigma_j n_j$, this can be defined as

$$\langle \sigma \nabla u_h \rangle := \frac{\delta_i}{\delta_i + \delta_j} \sigma_i \nabla u_h|_{E_i} \cdot n_i + \frac{\delta_j}{\delta_i + \delta_j} \sigma_j \nabla u_h|_{E_j} \cdot n_j$$

The factor $\tau_\gamma \in \mathbb{R}$ scales the penalty term at conductivity jumps on an edge $\gamma = \gamma_{i,j}$. It is defined as the harmonic average of δ_i and δ_j: $\tau_\gamma := 2\delta_i\delta_j/(\delta_i + \delta_j)$. To accommodate for different polynomial orders, the penalty term is scaled by $\nu_k = k(k+2) \in \mathbb{R}$ as described in [6]. Note that the bilinear form $a + J$ is symmetric. As a DG-FEM approach, this method is also called symmetric weighted interior penalty Galerkin (SWIPG) method [7]. If the penalty parameter is large enough, i.e., $\eta \geq \eta_0 > 0$ for a specific $\eta_0 \in \mathbb{R}$, the problem has a unique solution. Note that each integral can be replaced by a sum over cut cell local contributions.

In the following we will assume that the elements of the fundamental mesh are hexahedrons. We thus use $\mathbb{Q}_k(\overline{E})$ for the local polynomial spaces in V_h^k. On each cut cell, the local polynomial space is spanned by $N_b \in \mathbb{N}$ local basis functions $\varphi_0, \dots, \varphi_{N_b-1}$. For $k = 1$ we obtain $N_b = 8$ and for $k = 2$ we obtain $N_b = 27$ local basis functions respectively. By introducing a global numbering of the local basis functions and inserting these into the model, we can assemble a sparse linear equation system, which can be subsequently solved numerically. The integration over the cut cells and the skeleton is performed by a modified marching cubes algorithm. It creates a subtriangulation of a cut cells domain and its boundary consisting of simpler, polyhedral elements, where common quadrature rules such as Gaussian quadrature are available. A further explanation of this method can be found in [1], while a detailed study has been performed in [8]. The numerical solution u is evaluated at the electrode positions $x_0, \dots, x_{N_e-1}$ which results in a potential vector $U \in \mathbb{R}^{N_e}$. To reduce the computational load of solving the linear system for each dipole position, fast transfer matrix approaches are used (see e.g. [9]).

B. Source model

A common source model used for the EEG forward problem is the mathematical dipole with a moment $M \in \mathbb{R}^3$ and location $x_0 \in \mathbb{R}^3$. Using the mathematical dipole in the Poisson equation results in the source term $f = \nabla \cdot M\delta_{x_0}$, with the Dirac delta distribution δ_{x_0}. As this source term is highly irregular, we use the partial integration approach as an approximation. The resulting right hand side of the discretized model for a basis function φ_i then reads:

$$l(\varphi_i) \approx \begin{cases} -M \cdot \nabla\varphi_i(x_0) & , x_0 \in \text{support}(\varphi_i) \\ 0 & , \text{else} \end{cases} \tag{12}$$

C. Meshes

In order to compare the results of first and second order polynomials, we use a four-layer sphere model. For such a model geometry, quasi analytic solutions of the EEG forward problem can be provided [10]. The radii of the different spheres along with the conductivity values of the tissue compartments are given in Table I. For the conductivity values, we followed the recommendations of [11]. To obtain a fair comparison, the number of degrees of freedom (DOFs) for the first and second order models should be comparable. As the local polynomial spaces have a different number of

TABLE I: Sphere radii, tissue labels and conductivity values from outer to inner compartment.

Radius	92 mm	86 mm	80 mm	78 mm
Tissue	skin	skull	CSF	brain
Conductivity	0.43 S/m	0.01 S/m	1.79 S/m	0.33 S/m

TABLE II: Number of cut cells and thus number of degrees of freedom (DOFs) for the different cut cell models

degree	*N*	N^3	*cut cells*	*DOFs*
1	58	195.112	126.152	1.009.216
2	36	46.656	35.672	963.144

basis functions, we use different fundamental mesh sizes for both models. For the level set representations, both meshes where two times globally refinement to obtain a more accurate geometric representation. Note that the local basis function are still defined on the unrefined fundamental mesh. The number of elements, the resulting number of cut cells and thus the number of DOFs can be seen in Table II. The second order model has slightly less DOFs than the first order model. In the following, we will denote these models by UDG(1) 1009k and UDG(2) 963k for first and second order respectively.

D. Sources

We created two sets of test sources, one consisting of radial and the other of tangential dipoles. For each set, we generated 1000 dipoles on each of 10 eccentricities in the inner compartment, scaled logarithmically towards the first conductivity jump. The most eccentric sources where located at a distance of 0.48mm from the boundary of the inner compartment, which corresponds to an eccentricity of 0.9939.

E. Error measures

The error of a numerical solution $U_{\text{num}} \in \mathbb{R}^{N_e}$ evaluated at the electrodes and an analytic solution $U_{\text{ana}} \in \mathbb{R}^{N_e}$ is measured by the *relative difference measure* (RDM%) and the *magnitude error* (MAG%) which are defined as.

$$\mathrm{RDM\%}(U_{\text{num}}, U_{\text{ana}}) = \frac{100}{2} \left\| \frac{U_{\text{num}}}{\|U_{\text{num}}\|} - \frac{U_{\text{ana}}}{\|U_{\text{ana}}\|} \right\| \quad (13)$$

$$\mathrm{MAG\%}(U_{\text{num}}, U_{\text{ana}}) = 100 \left(\frac{\|U_{\text{num}}\|}{\|U_{\text{ana}}\|} - 1 \right) \quad (14)$$

The error given by both measures is better, the closer it is to 0. The results are presented as box plots (see Fig. 1), where a black horizontal line shows the median, a colored box shows the interquartile range (IQR) and vertical black lines show the total range (TR) for a given source eccentricity.

III. RESULTS

In this study we compared the first order to the second order UDG-FEM method in a four-layer sphere model. The RDM% and MAG% statistical errors can be seen in Fig. 1. For both, radial and tangential dipoles and first and second order, we observe an increasing RDM% error and an increasing total range (TR) of the MAG% error for higher eccentricities. The maximal RDM% error and the median RDM% value of each eccentricity of UDG(2) is below the respective value of UDG(1). The interquartile range (IQR) of the RDM% error of UDG(2) is always below the one of UDG(1). The maximal RDM% error and the maximal abolute value of the MAG% error for radial and tangential dipoles with eccentricities below 0.95 can be seen in Table III. Up to an eccentricity of 0.95, the MAG% error for radial dipoles of UDG(2) has a smaller TR and IQR than UDG(1) and the median values are closer to 0. Above an eccentricity of 0.95, the MAG% error for both methods show a stronger increase in TR and IQR and both methods perform similarly. Above an eccentricity of 0.95, the TR of the RDM% error for UDG(2) increases, but the median and IQR are still below the respective values of UDG(1). The TR and IQR of the MAG% error for tangential dipoles of UDG(2) are overall smaller than the ones of UDG(1) and the median values are closer to 0.

TABLE III: Maximal RDM% error and maximal absolute value of MAG% error of UDG(1) and UDG(2) for radial and tangential dipoles with an eccentricity below 0.95.

	radial		*tangential*	
method	RDM%	|MAG%|	RDM%	|MAG%|
UDG(1)	1.96 %	3.63 %	1.83 %	2.76 %
UDG(2)	0.45 %	2.35 %	0.44 %	0.88 %

IV. DISCUSSION

In this paper, we presented a study of second order polynomials in the unfitted discontinuous Galerkin finite element method (UDG-FEM) for solving the EEG forward problem. We recalled the mathematical formulation of the underlying model and described differences to the first order model. We performed a comparison of the first order UDG-FEM, (UDG(1)) to the second order method (UDG(2)) in a multi-layer sphere model. Both methods had approximately the same number of degrees of freedom. The second order method showed overall better results than the first order model. Only for sources with a higher eccentricity, the MAG% error for radial dipoles and the RDM% error for tangential dipoles where not influenced as strong as for the remaining sources. In [1] an extensive study of the UDG-FEM method has been performed. It was compared to a DG-FEM method on hexahedral and conforming tetrahedral meshes and the geometric representation of the model could be identified as a main error source. By maintaining the good approximation of the geometry of UDG-FEM we can show a benefit of the better approximation quality of the higher polynomial order.

For the standard finite element approach on conforming tetrahedral meshes, second order finite elements have been studied [3]–[5]. An increase in the approximation quality could be found in these studies, while it was concluded that with a better geometric representation of the different tissue compartments, the effect might be more pronounced. We obtain similar results with regard to the increasing accuracy for a second order method.

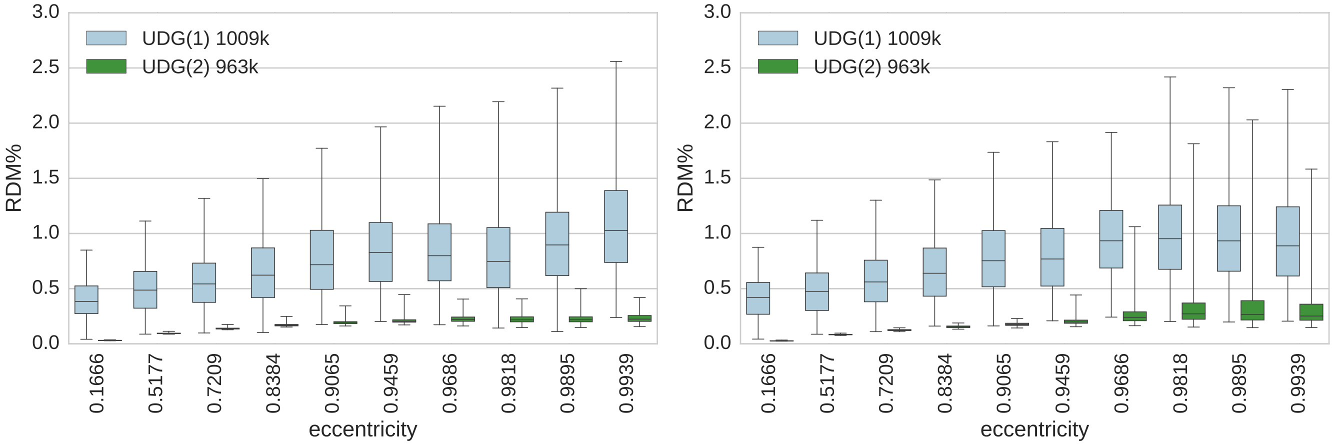

(a) RDM% error for radial dipoles

(b) RDM% error for tangential dipoles

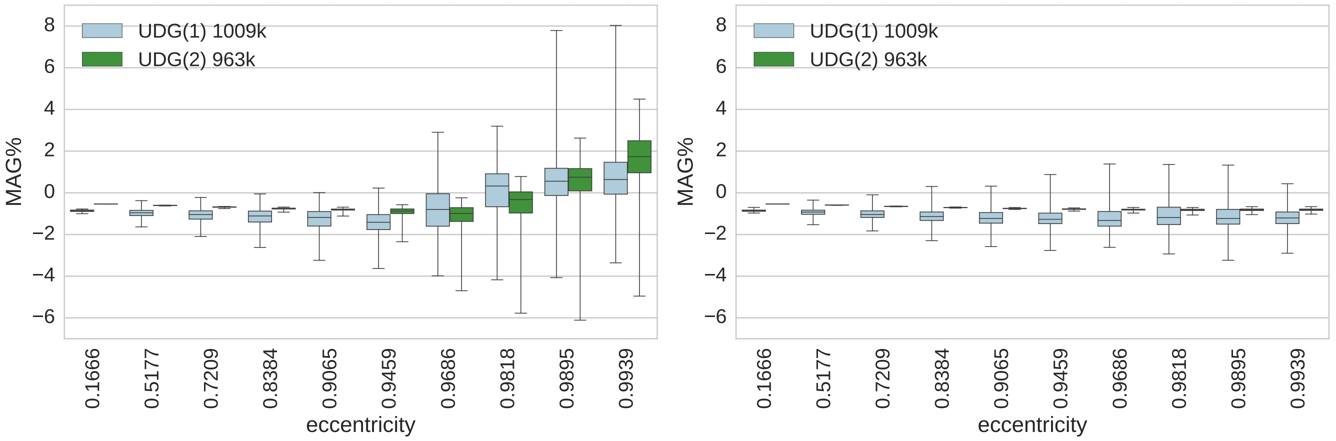

(c) MAG% error for radial dipoles

(d) MAG% error for tangential dipoles

Fig. 1: Comparison of the first (light blue) and second (green) order UDG-FEM model: RDM% (upper row) and MAG% (lower row) errors for radial (left column) and tangential (right column) sources. Note that the x-axis is logarithmically scaled.

V. CONCLUSION

We presented a study of the unfitted discontinuous Galerkin method for solving the EEG forward problem with second order polynomials. Second order polynomials could achieve a better accuracy while using the same number of degrees of freedom compared to linear polynomials.

ACKNOWLEDGEMENT

This work was partially supported by the Cluster of Excellence 1003 of the Deutsche Forschungsgemeinschaft (DFG EXC 1003 Cells in Motion), by EU project ChildBrain (Marie Curie Innovative Training Networks, grant agreement no. 641652) and by the Priority Program 1665 of the Deutsche Forschungsgemeinschaft (DFG) (WO1425/5-1).

REFERENCES

[1] A. Nüßing, C. H. Wolters, H. Brinck, and C. Engwer, “The Unfitted Discontinuous Galerkin Method for Solving the EEG Forward Problem,” *ArXiv e-prints*, Jan. 2016, submitted, arXiv:1601.07810.

[2] P. Bastian and C. Engwer, “An unfitted finite element method using discontinuous Galerkin,” *Int. J. Numer. Methods Eng.*, vol. 79, no. 12, pp. 1557–1576, 2009.

[3] Y. C. Zhang, S. A. Zhu, and B. He, “A second-order finite element algorithm for solving the three-dimensional EEG forward problem,” *Phys. Med. Biol.*, vol. 49, no. 13, p. 2975, 2004.

[4] R. Van Uitert, D. Weinstein, C. Johnson, and L. Zhukov, “Finite Element EEG and MEG Simulations for Realistic Head Models: Quadratic vs. Linear Approximations,” *Biomedizinische Technik/Biomedical Engineering*, vol. 46, no. s2, pp. 32–34, 2009.

[5] F. Grüne, “Validierung von FEM-Ansätzen höherer Ordnung für das EEG-Vorwärtsproblem,” Master thesis, Fachbereich Mathematik und Informatik, Westfälische Wilhelms-Universität Münster, Germany, 2014.

[6] Y. Epshteyn and B. Rivière, “Estimation of penalty parameters for symmetric interior penalty Galerkin methods,” *Journal of Computational and Applied Mathematics*, vol. 206, no. 2, pp. 843–872, Sep. 2007.

[7] A. Ern, A. F. Stephansen, and P. Zunino, “A discontinuous Galerkin method with weighted averages for advection–diffusion equations with locally small and anisotropic diffusivity,” *IMA J. Num. Anal.*, 2008.

[8] C. Engwer and A. Nüßing, “Geometric integration over irregular domains with topologic guarantees,” *ArXiv e-prints*, Jan. 2016, submitted, arXiv:1601.03597.

[9] D. Weinstein, L. Zhukov, and C. Johnson, “Lead-field bases for electroencephalography source imaging,” *Ann. Biomed.Eng.*, vol. 28, no. 9, pp. 1059–1066, 2000.

[10] J. de Munck and M. J. Peters, “A fast method to compute the potential in the multisphere model,” *IEEE Trans.Biomed.Eng.*, vol. 40, no. 11, pp. 1166–1174, 1993.

[11] M. Dannhauer, B. Lanfer, C. H. Wolters, and T. R. Knösche, “Modeling of the human skull in EEG source analysis,” *Human Brain Mapping*, vol. 32, no. 9, pp. 1383–1399, 2011.